Kaolinite flocculation structure

Marek S. Zbik [a,1], Roger St.C. Smart [b,*], Gayle E. Morris [a,2]

[a] Ian Wark Research Institute, University of South Australia, Mawson Lakes, South Australia 5095, Australia
[b] ACeSSS (Applied Centre for Structural and Synchrotron Studies), University of South Australia, Mawson Lakes, South Australia 5095, Australia

ARTICLE INFO

ABSTRACT

Effective flocculation and dewatering of mineral processing streams containing colloidal clays has become increasingly urgent. Release of water from slurries in tailings streams and dam beds for recycle water consumption, is usually slow and incomplete. To achieve fast settling and minimization of retained water, individual particles need to be bound, in the initial stages of thickening, into large, high-density aggregates, which may sediment more rapidly with lower intra-aggregate water content. Quantitative cryo-SEM image analysis shows that the structure of aggregates formed before flocculant addition has a determinative effect on these outcomes. Without flocculant addition, 3 stages occur in the mechanism of primary dewatering of kaolinite at pH 8: initially, the dispersed structures already show edge–edge (EE) and edge–face (EF) inter-particle associations but these are open, loose and easily disrupted; in the hindered settling region, aggregates are in adherent, chain-like structures of EE and stairstep face–face (FF) associations; this network structure slowly partially rearranges from EE chains to more compact face–face (FF) contacts densifying the aggregates with increased settling rates. During settling, the sponge-like network structure with EE and FF string-like aggregates, limits dewatering because the steric effects in the resulting partially-gelled aggregate structures are dominant. With flocculant addition, the internal structure and networking of the pre-aggregates is largely preserved but they are rapidly and effectively bound together by the aggregate-bridging action of the flocculant. The effects of initial pH and Ca ion addition on these structures are also analyzed. Statistical analysis from cryo-SEM imaging shows that there is an inverse correlation of intra-aggregate porosity with Darcian inter-aggregate permeability whereas there is a strong positive correlation of Darcian permeability with settling and primary dewatering rate as a function of pH in suspension. Graphs of partial void contributions also suggest that it is not total porosity that dominates permeability in these systems but the abundance of larger intra-aggregate voids.

© 2008 Elsevier Inc. All rights reserved.

1. Introduction

Flocculation and dewatering of slurry streams containing significant proportions of clays is becoming increasingly urgent in view of the growing demand for high density disposal of mining slurries, tailings and other mineral wastes. Mine tailings are usually disposed of as high water content slurries (e.g. >75 wt%) into tailing dams. Release of water, for recycle and reduced make-up water consumption, from these slurries in tailings streams and beds is usually slow and incomplete. Because clay particles are extremely small, generally <200 nm in lateral dimension, natural separation by sedimentation, governed by Stoke's law, is very slow. For instance, clays as kaolinite and smectites largely determine the primary dewatering of tailings from coal, iron ore, heavy minerals and some base metal sulfide operations.

Primary dewatering processes include aggregate formation, bridging flocculation, settling rate and bed height (density) before compression. Aggregation is usually understood to be achieved by flocculation using long chain polymers but this process is not well understood. Our research, derived from the direct imaging and quantitative measurement of aggregate structures described in this paper, has shown that this understanding is incomplete and, in some respects, misleading. The structure of aggregates formed before flocculant addition can be determinative of the sedimentation rate, the final bed density and the retained water after drainage.

It is well established in both theory and practice that changes in settling rates and solids density of tailings containing clays can be

* Corresponding author. Fax: +61 8 83025545.
E-mail addresses: m.zbik@qut.edu.au (M.S. Zbik), roger.smart@unisa.edu.au (R.St.C. Smart), gayle.morris@vu.edu.au (G.E. Morris).
[1] Present address: Inorganic Materials Research Program, School of Physical and Chemical Sciences, Queensland University of Technology, GPO Box 2434, Brisbane, QLD 4001, Australia.
[2] Present address: Office for Research, Victoria University, PO Box 14428, Melbourne, Victoria 8001, Australia.
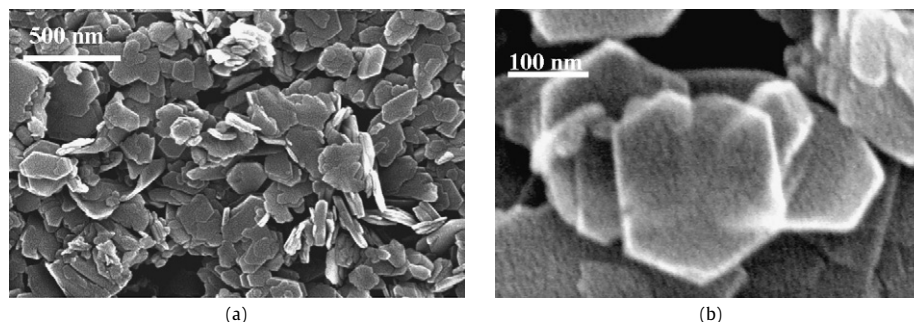
Fig. 1. High resolution SEM micrographs of the clay fraction of kaolinite K15GM.

achieved in practice by changes in pH, dissolved cations and flocculant additions. Contemporary approaches to control dilute clay suspension are based on colloid stability theory developed by Derjaguin and Landau [1] and Verwey and Overbeek [2], known as the DLVO theory, where competing electrostatic and van der Waals forces generally decide whether particular colloid clay suspensions will be stabilized (in sol form) or coagulated (in gel form). On this basis, Hogg [3] described opportunities for control of floc characteristics by physical displacement between particles, chemical changes in pore electrolyte, and introduction of new mineral phases into the system. All of these manipulations may collapse the electrical double layer which will lower the electrokinetic potential and allow particles close enough for van der Waals forces to bond particles into larger aggregates which significantly increase settling rates. To be successful, these manipulations require initial dispersion of the clay particles in suspension.

Based on Hogg's review [3] and our results, the initial proposition can be put forward that, to achieve fast separation of clays from water and minimization of retained water, individual particles need to be bound into high-density, low-internal-porosity aggregates before flocculant addition, which may then sediment more rapidly with lower intra-aggregate water content. To build these aggregates, specific structures must be developed in the clay suspension in the initial stages of thickening. This pre-flocculant structure is determined by the mineral surface structure and chemistry together with the solution chemistry. Our previous experience with SEM/AFM studies on clay mineral morphology and texture has played an important role in understanding platelet shape, aspect ratio, roughness of the basal planes of platelets and the role of floc porosity in structure-forming phenomena [4–7]. The second part of the proposition is that, with flocculant addition, the internal structure and networking of the pre-aggregates is largely preserved but they are rapidly and effectively bound together by the bridging action of the flocculant(s) to produce larger, linked aggregates that sediment fast. Provided that the flocculant is chosen to give effective adsorption (charge) and bridging (length, charge density), it is the pre-flocculant structure that requires optimization for most effective water exclusion.

The evidential basis of this proposition comes from the development of a very useful technique involving cryo-vitrification of slurry structure followed by partial sublimation of vitrified water and cold stage SEM to image low density floc structures directly. This has enabled the measurement of porosity and the calculation of permeability from the SEM images using STIMAN (STructural IMage ANalysis). STIMAN quantitative image analysis software was developed in Professor Sokolov's group at Moscow State University [8–11]. This method, initially designed to study structure in porous rocks [12], has since been adapted for application to clay aggregate systems [13,14].

2. Materials and methods

2.1. Kaolinite

Commercial Minerals Ltd. (now Unimin Australia P/L) kaolinite K15GM produced at Adelaide, South Australia from their Birdwood quarry, surface area 19.7 m^2/g was used. XRD description of this sample has been given in Frost et al. [15]. A detailed description of the Birdwood kaolinite investigation and comparison with Georgia kaolinite using cryo-SEM has been given in [6,7]. SEM characterization of the mineral particles is illustrated in Fig. 1. The kaolinite is generally represented as pseudo-hexagonal or euhedral crystals with diameters down to ∼50 nm (Fig. 1). The crystals are typically thin and flexible plates. AFM investigations of this kaolinite [6] show that crystals are on average 160 nm in diameter and ∼13 nm thick giving aspect ratio values ∼12 [4,5]. A few grape-shaped anatase aggregates and tubular halloysite particles are also present (Fig. 1).

2.2. Zeta potential

Electrokinetic (zeta) potential was measured as a function of pH using AcoustoSizer II (Colloidal Dynamics) in 0.01 M NaCl in 6 wt% kaolinite suspension. The zeta potential of this material presented in Fig. 2 displays negative zeta potential values with a pH-dependent profile due to surface hydroxyl groups present at the platelet edges [16]. This kaolinite has a relatively high measured gel point (GP) in the range 10–12 wt%.

2.3. Flocculant

The anionic polyacrylamide flocculant, A-130, an acrylamide–acrylic acid random copolymer was obtained courtesy of Cytec Industries, USA. A-130 has a molecular weight of 12×10^6 Da and an acrylic acid monomer content of approximately 35%. The flocculant dosages ranged from 0 to 0.029 mg/m^2 (∼600 g/tonne).

High-purity water was produced by the following sequential treatments: reverse osmosis, two stages of mixed bed ion exchange, two stages of activated carbon treatment and a final filtering step through a 0.22 μm filter. The conductivity was less than 0.5 μS/cm with a surface tension of 72.8 mN/m at 20 °C.

2.4. Cryo-SEM analysis

In the cryo-vitrification SEM studies, the sample is taken by a large-aperture (>2 mm) pipette directly from the flocculating system at chosen times and depths, e.g. immediately after dispersion, from the top, middle or bottom of the sedimenting column or from the top of the settled bed. The sample is immediately plunged into a Dewar of liquid propane, cooled by liquid nitrogen, which reduces the temperature at >1000 °C/min freezing the water without allowing crystallization, i.e. vitrifying [17]. Vitrified
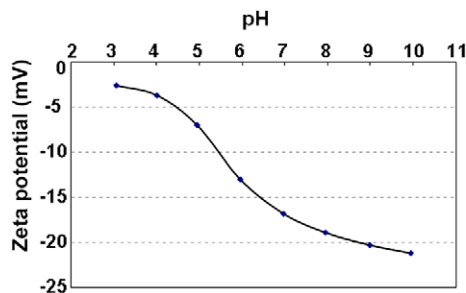
Fig. 2. Zeta potential of kaolinite K15GM in 0.01 M NaCl as a function of pH measured using the AcoustoSizer II instrument.
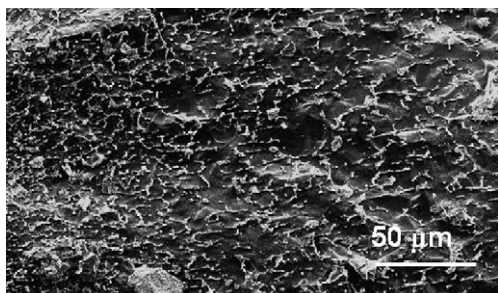

Fig. 3. Low magnification cryo-SEM micrograph of a 4 wt% kaolinite suspension showing the cellular, extended structure of chained kaolinite aggregates.

samples are placed onto the liquid nitrogen-cooled specimen stage of the field emission scanning electron microscope Philips XL30 FESEM with Oxford CT 1500HF Cryo stage. The sample is fractured under vacuum and a small amount of vitrified H_2O sublimed off by raising the stage temperature to $-90\,°C$ for ~ 30 s (removing ~ 240 nm, i.e. much less than the dimensions of the aggregate structures) then lowering back to $\sim -180\,°C$. This technique exposes the structure of the snap-frozen aggregates proud of the surface of the vitrified water greatly improving imaging and quantitative image analysis. Finally a 3 nm gold or palladium, high resolution coating is evaporated on to the exposed surface to increase conductivity before SEM imaging.

2.5. STIMAN analysis

A typical low magnification secondary electron micrograph of a low solids kaolinite suspension is presented in Fig. 3 showing kaolinite platelets (bright) protruding from vitrified water (dark) illustrating the structures that can be observed in this preparation. These images can be statistically analyzed using the STIMAN program. The STIMAN image analysis [8–11] has the unique feature that it allows study of polydispersed samples by combining a series of SEM images at different magnifications, covering the entire range of particle and aggregate sizes under investigation. STIMAN combines images across magnifications of $250\times$, $500\times$, $1000\times$, $2000\times$, $4000\times$, $8000\times$ and $16,000\times$. Micrographs at higher magnifications were used for morphology description. The micrograph series of magnifications $500–8000\times$ were used exclusively to calculate microstructural parameters using the STIMAN image analyzing program. Hence, we can extract integrated information on sample microstructure, especially on total pore (void) space and the spread of micropore sizes. This program contains a new subroutine for estimating filtration properties from the void space. Examples of the output parameters include: number of voids analyzed; porosity (%); total void area (sq. μm); total void perimeter (μm); average diameter (μm)/dispersion; average area (sq. μm)/dispersion; average perimeter (μm)/dispersion; specific area (1/μm), permeability (mD).

3. Theory and calculations

To consider settling data in relation to permeability and dewatering, Darcian theory is usually the starting point. In dewatering of a suspension, two regions of behavior exist—at high solids, a particle network is formed spanning the vessel with compressive strength; at low solids, inter-particle contact occurs but a spanning network is not formed. The transition is the gel point ϕ_g [18]. Darcian filtration $k(\phi)$ represents the inter-aggregate dewatering potential and is measured by the hindered settling function $R(\phi)$ which takes into account the hydrodynamic interactions between aggregates increasing drag during the first stage of settling. The relationship between dewatering parameters from traditional Darcian, fluid mechanical and geotechnical theories has recently been reviewed by de Kretser and Scales [19].

Below the gel point, in initial settling before compression, the two relevant equations are:

$$R(\phi) = \Delta\rho g(1-\phi_0)^2/S_i, \tag{1}$$

where $\Delta\rho$ is the solid–liquid density difference, ϕ_0 is the initial solids volume fraction and S_i is the initial settling rate and

$$k(\phi) = \eta/R(\phi)(1-\phi)/\phi, \tag{2}$$

where η is the viscosity of the solid-solution at the volume fraction ϕ. Hence we can estimate the Darcian inter-particle permeability $k(\phi)$ below the gel point from measurement of the initial settling rate and the viscosity of the suspension. This will allow comparison between Darcian inter-aggregate permeability and intra-aggregate permeability estimated from cryo-SEM STIMAN image analysis.

For STIMAN intra-aggregate permeability calculation, defined as isometric pores connected with thin channels [12], we used pore equivalent diameter D_i and porosity m_i with the Kotyakhov formula [12] to calculate the permeability index K in units of Darcy, i.e. μm².

$$K = 0.061\Sigma D_i^2 m_i^{2.1}, \tag{3}$$

where the summation is over pore diameters up to D_{cr}, the critical diameter corresponding to the boundary between the intra-aggregate thin channels and the inter-aggregate larger pores. This boundary is illustrated in calculations discussed in Section 4.6.

In the STIMAN program, filtration is calculated in mili-Darcy (mD) which for water as the liquid medium, $K = 1$ Darcy corresponds to a filtration $K_f = 0.036$ m/h. This conversion factor has been used to calculate the filtration discussed in the paper.

4. Results and discussion

4.1. Settling rates and permeability/dewatering

Conventional settling rate column tests have been conducted in cylinders as described in [20]. The settling of kaolinite without flocculant at pH 8 and solid mass density 4 wt% is illustrated in Fig. 4. Particles are in the coagulation stage which means no individual particles have been observed above the clearly defined "mudline." Three significant stages (Figs. 4a, 4b, 4c) of aggregate formation have been observed during this process to be described in the next section. It is significant that, after the initial induction period (a), the settling height plots are continuously curved (Fig. 4) suggesting that the clays in suspension have formed an interacting network inhibiting settling. This view is also supported in the mechanism proposed by Nasser and James [21] but this network has not been directly observed.

Examples of data for kaolinite tests at different pH with flocculant addition are shown in Fig. 5. The flocculant dosage may
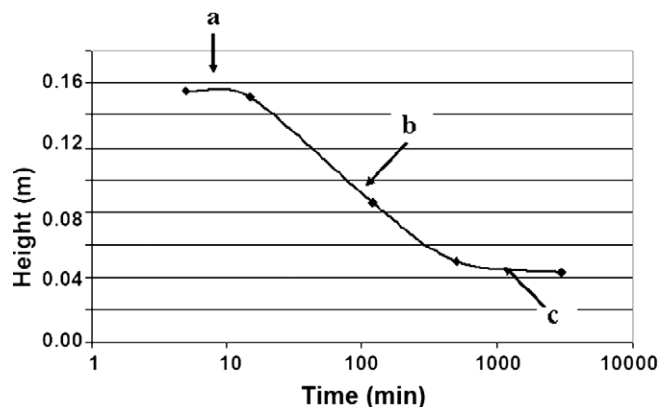
Fig. 4. Settling curve and associated aggregate structures (Fig. 6) for 4 wt% kaolinite suspension at pH 8 in 0.01 M NaCl in the absence of flocculant.
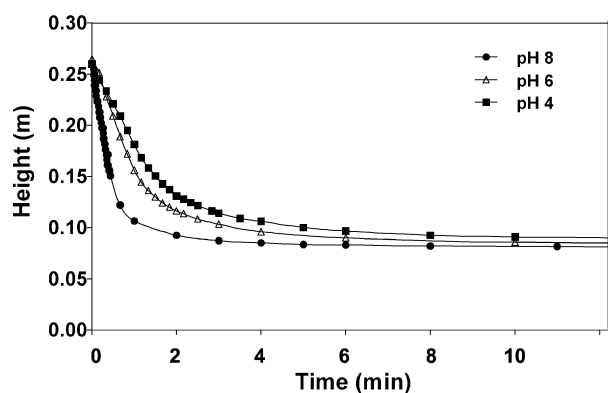

Fig. 5. Settling curves as a function of pH for 4 wt% kaolinite in the presence of 0.029 mg/m^2 A-130 flocculant in 0.01 M NaCl.

Fig. 6. Enlarged cryo-SEM micrographs from Fig. 4 corresponding to: (a) first sample dispersed stage; (b) second stage pseudo-gelled chain structures; and (c) third stage FF-compacted structures.

appear to be large but, to put this in context for tailings (surface area 5 m^2/g) with 60% kaolinite, a dosage of 0.029 mg/m^2 corresponds to ∼45 g/tonne which is within industry norms. In these examples of results, the fastest (initial) settling rate and the highest bed density are found at pH 8. The settling rate and bed height at pH 10 (not shown) lie between pH 8 and 6. The settling times to initial bed formation are much shorter (<5 min) compared with kaolinite without flocculant (>1000 min).

4.2. Kaolinite aggregation: No flocculant

Fig. 6 shows typical SEM images of the aggregate structure from the three different stages (Figs. 6a, 6b and 6c) of settling for a 4 wt% kaolinite suspension in pH 8 and 0.01 M NaCl without flocculant addition. In Fig. 6a, taken at the earliest possible stage of dispersion, the structures already show edge–edge (EE) and edge–face (EF) inter-particle associations but these are open, loose and easily disrupted. These particles and loose aggregates are already flocculated but dispersed according to the Van Olphen [22] model. These structures do not accord with electrostatic DLVO theory where both the kaolinite basal planes and edge sites are negatively charged at pH 8 [16] but van der Waal's forces in the near potential minimum can induce coagulation if the charge barrier can be overcome [23]. A calculation by Babak and Sokolov [24] of these forces acting between edges and faces of kaolinite particles, dependent on pH and salt concentration, has been evaluated for the aggregate structures. Their work has shown that the aggregate structural strength decreases near the isoelectric point for the edge sites at pH 7 suggesting that approach to the near potential minimum may be possible under these conditions.
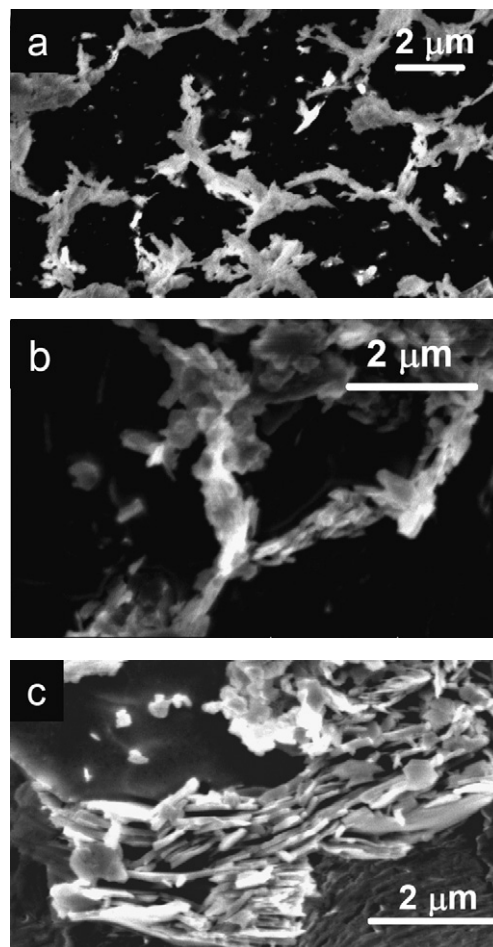
After some induction time (which varies with solid loading and electrolyte characteristics), settling starts (Fig. 6b), the solids density in the settling region is still below the GP (∼0.6) but the aggregates are now arranged into chain-like structures of EE and stairstep face–face (FF) associations apparently quite strongly adherent. Similar stair-step chain aggregates, building cardhouse-like structures, have been observed previously by O'Brien [25,26] using freeze-drying techniques however this technique can readily alter the structure during drying. In the third stage (Fig. 6c), individual platelets in EE and FF stepped arrangements as chains, appear to slide across each other to more FF structures forcing the chain aggregates to contract. This contraction leads to fragmentation of the previously extended network and formation of compact aggregates. The images suggest that the solids density within each chain is likely to be well above the gel point GP. Nevertheless, this structure remains largely suspended apparently because it does not bridge the vessel and confer a compressive resistance. The settling rate in this stage is high and can exceed those expected by Stoke's law from relatively large particles >20 μm diameter of kaolinite density (although the aggregates are likely of much lower density). The dramatic increase in settling rate is likely to be enhanced by the FF compact aggregate formation. A mechanism for the chain aggregate rearrangement observed by cryo-SEM micrographs (Fig. 6c) is still unknown. The platelets appear to slide across each other, despite their negative zeta potential, suggesting hydrophobic or van der Waal's forces are involved at these very close distances of approach.

The second stage, where sponge-like chain structures with predominantly EE oriented particles, are found, likely limits slurry dewatering because the steric van der Waal's effects in the resulting partially-gelled structure (Fig. 6b) are clearly more dominant than the electrostatic effects in DLVO theory. As particles slide across each other in the advancing stages, the particle orientation changes from EE to FF. The previously extended network contracts, and when the solid volume fraction is low, the continuous network breaks apart forming aggregates and aggregate associations (Fig. 6c) which are able to freely settle. These dense structures settle at increased rate, give lower bed density retaining less water after drainage. Nevertheless, without flocculant, settling is very slow (>1000 min).

Nasser and James [21] have also found supporting evidence in their study of kaolinite settling without flocculant. In basic pH ranges, the particles settle in both dispersed form (in low electrolyte concentration) and flocculated form (in high electrolyte concentration). The gel point and sediment bed behavior are found to be very sensitive to the type of inter-particle interactions. From their settling studies, they infer that FF flocculation produces higher gel points and higher apparent maximum packing fractions while EF flocculation produces higher compressive yield stresses at all volume fractions. Their results show good correlations between the settling behavior, gel point, and compressive yield stress for the different kaolinite particle interactions.

### 4.3. Influence of flocculant addition on structure

The cryo-SEM results (Fig. 7) show that the addition of anionic flocculant at pH 6 does not change the kaolinite particle orientation within the aggregates but rather causes the micro-aggregates to associate, apparently by bridging flocculation, giving larger macro-aggregates some mm in extent. Fig. 7c shows similar EE oriented, chain aggregates as those observed prior to flocculation (Fig. 7a) with the difference being that the chains are now cross-linked to other similar aggregates forming large flocs. In other words, flocculant addition to kaolinite suspensions "freezes"

the pre-existing particle structure and orientation. This mechanism does not appear to be widely acknowledged in the literature of clay flocculation. It has important implications for final bed density and dewatering without disruption of floc structures because both inter- and intra-aggregate water remains locked in the pre-flocculant structures. In practice, raking the flocculated bed is normally used to release some of this retained water but the % solids is still low in most tailings disposal.

The flocculant addition appears to lock the second or third stage pre-flocculant structure (Figs. 6a and 6b) before transition to a denser FF fourth stage macro-floc structure. Whilst this may not be universally true for other systems, it is consistent with the action of the flocculant bridging the existing aggregate structures without significantly altering their internal or inter-particle structure. The effect of the flocculant is then primarily to make larger, locked inter-aggregate structures that sediment faster at least until the GP is reached. However, the intra-aggregate water trapped in the initial structures is probably retained in this process if the denser FF aggregates do not have time to form prior to flocculant addition.

4.4. Influence of calcium ions

The addition of divalent cations is known to increase settling rates, but not bed densities, in kaolinite dispersions [3]. Fig. 7a shows kaolinite dispersed in 0.01 M NaCl solution and in Fig. 7b kaolinite is dispersed in 0.00025 M $CaCl_2$ solution. The addition of Ca(II) without flocculant clearly increases particle aggregation compared with Na(I) addition (Figs. 7a, 7b). In the presence of Ca(II) cations, the 2–5 µm aggregates look secondary and consist of individual particles aggregated mostly in a EF and EE orientations. The aggregates are often butterfly shaped with a number of platelets connected along one of the edges or stuck to the face of another platelet. Individual particles (0.3 µm long) are also present. Neither aggregates nor individual particles are connected into a spanning network. Intra-aggregate pore diameters calculated from SEM images using STIMAN are small (0.54 µm) and the spaces be-
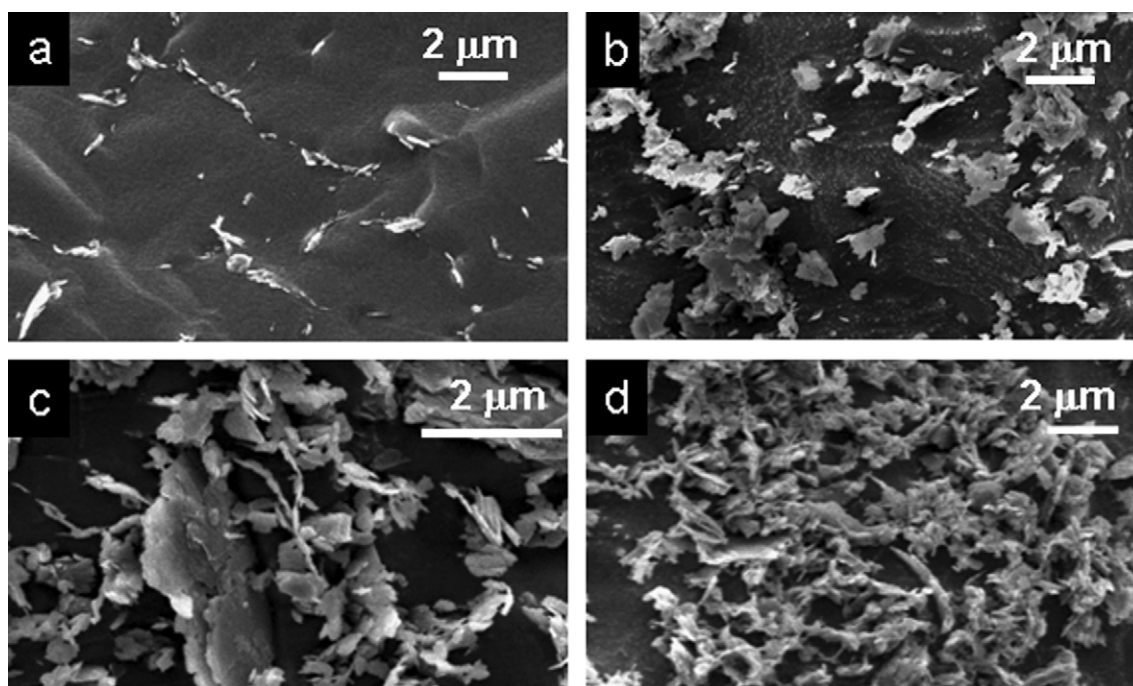
Fig. 7. Cryo-SEM micrographs from kaolinite suspension in the absence (a and b) and presence (c and d) of A-130 flocculant as a function of cation solution type at pH 6: (a) Na(I), no flocculant; (b) Ca(II), no flocculant; (c) Na(I), flocculant; and (d) Ca(II), flocculant. Sampling occurred near the top of the sediment bed. 0.01 M NaCl or 0.00025 M $CaCl_2$, 0.029 mg/m² A-130.
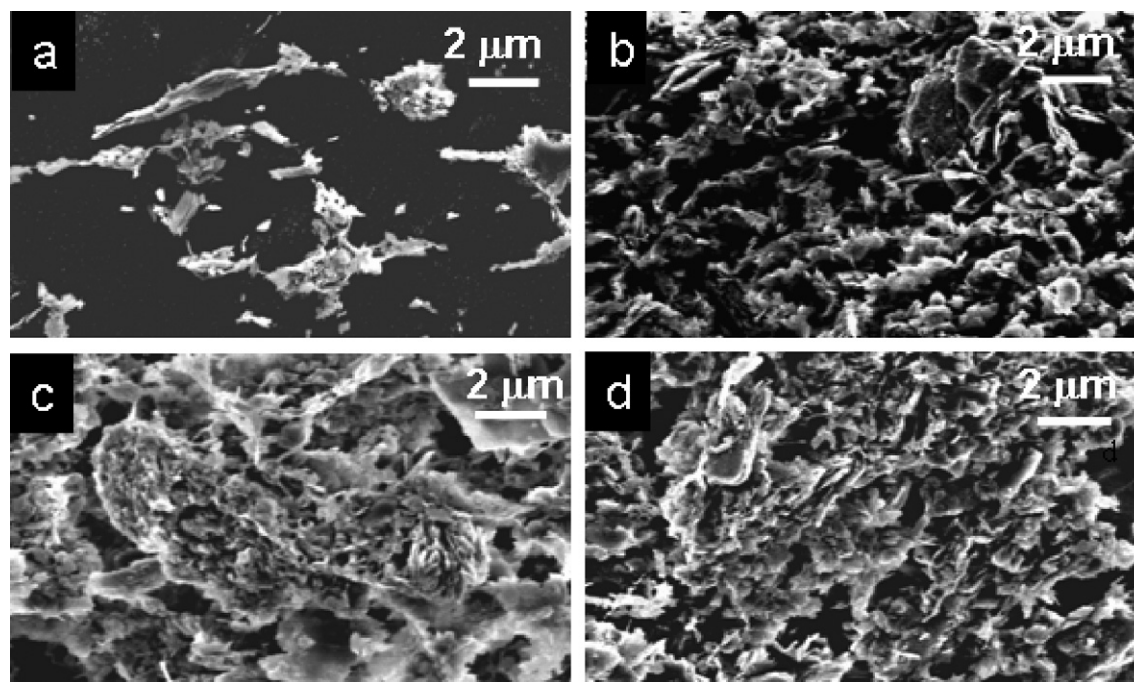
Fig. 8. Cryo-SEM micrographs from flocculated kaolinite samples as a function of pH: (a) 4; (b) 6; (c) 8; (d) 10. Sampling occurred near the top of the sediment bed.

tween aggregates (inter-aggregate pores) are up to 20 µm diameter and broadly distributed. A low average pore hydraulic diameter within aggregates influences the filtration coefficient within aggregates which are consequently very low, similar to other kaolinite suspensions without flocculant addition. But as the micrograph in Fig. 7b suggests, because of the presence of larger inter-aggregate voids and channels, the kaolinite suspension permeability index, in the presence of Ca(II) ions, is an order of magnitude larger than that when Na(I) ions are present. This can also be an effect of the different aggregate structure in Ca(II) solution where the voids inside the aggregates are larger than in case of monovalent ions presence, due to the rather EF particle orientation which differs from the nano-size voids in the extended EE oriented aggregates in the Na(I) solution.

In the presence of Ca(II) ions with flocculant, as shown in Fig. 7d, the particle orientation has been preserved with aggregates cross-linked to form flocs which are obviously larger than the pre-existing aggregates but are not obviously denser. The trapped pore spaces inside the micro-aggregates in the presence of calcium ions are smaller but more extensive than in the presence of Na(I) ions (Fig. 7c). This difference appears to reflect the different particle orientation within the aggregates of both systems before flocculant addition.

The total area in Fig. 7d shows three distinctive pore categories. The first category represents sub-micrometer pores which may be related to inter-particle volume spaces within the micro-aggregates. The second category consists of pores between 2 and 20 µm which contain volumes between micro-aggregates. The third category relates to larger inter-aggregate channels with diameters 50–100 µm.

4.5. Influence of pH

Kaolinite 4 wt% suspensions, prepared over a range of pH values before flocculant addition, show microstructural difference as defined by particle arrangement (Fig. 8). Differences in the aggregate structures of the flocculated material, in the presence of flocculant, as a function of pH are consistent with the behavior of the flocculant as the net charge alters. This can be observed in the sequence

of SEM micrographs of flocculated kaolinite at the different starting pH values of 4, 6, 8 and 10, as presented in Fig. 8. The samples are taken from close to the top of the sedimented bed, i.e. at the final stages of flocculation above the GP.

At pH 4 (Fig. 8a), the aggregates appear to be largely separate, loose, disordered associations consisting of mainly EE (with some EF and FF) short chain structures a few µm long, often only single kaolinite platelets in thickness, but they are apparently not adherent. The structure has a high void ratio. This is consistent with the relatively low or neutral surface charge on the adsorbed anionic polymer at this pH [20], adsorbed flat to the surface and unable to extend between aggregates inhibiting the settling rate. At pH 6 (Fig. 8b), a very different linked, porous aggregate structure is observed with much more EE and FF chain development but still some EF disorder. The structure is more compact than pH 4 but appears likely to be still relatively flexible. The chain aggregates appear to build a cellular spanned network, within the frame of the image. At pH 8 (Fig. 8c), there is more densification near the top of the bed with EE and now FF compaction clearly evident. The structure is still porous on the meso-pore scale but the intra-aggregate micropores appear smaller. At pH 10 (Fig. 8d), the structure is quite similar to pH 8 but may have started to open out again with an apparent increase in disorder of the chains likely to be due to the increasing negative net charge on the anionic polymer [20]. EE and FF stacking dominate the pH 10 structure but the region at lower right in Fig. 8d illustrates this increasing disorder as the settling rate and bed density decrease from those at pH 8.

4.6. Porosity–permeability-dewatering correlations

It has recently become possible using advanced image analysis software to examine the cryo-SEM micrographs of aggregate porosity and permeability in these different pH systems [12–14]. Fig. 9 summarizes the STIMAN porosity analysis with comparison to the settling rates for each pH system. In this analysis, closed porosity is calculated from void (dark areas in micrographs) regions completely bounded by (light areas in micrographs) particles and open porosity is calculated from void regions that are not completely
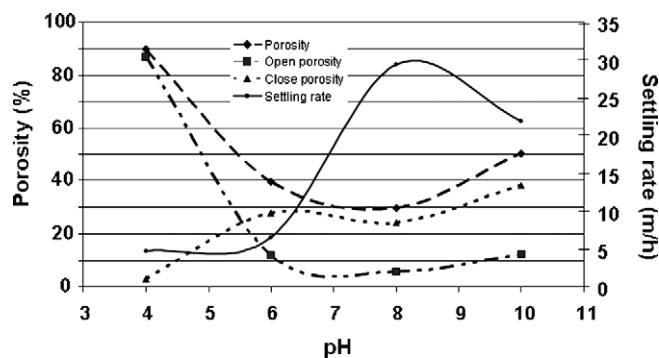
Fig. 9. STIMAN porosity analysis of flocculated kaolinite samples as a function of pH.
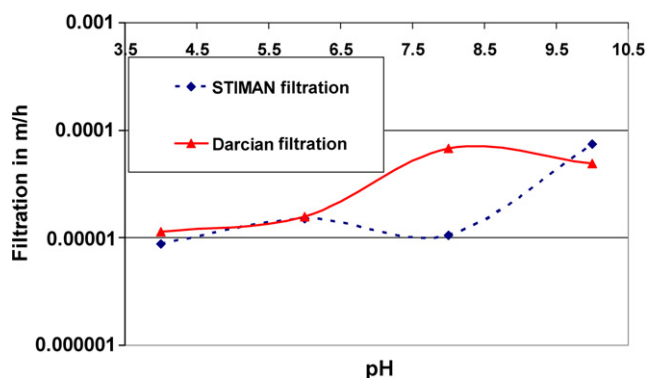

Fig. 10. Flocculated kaolinite filtration calculated using Darcian parameters (Eq. (2)) compared with those from STIMAN image analysis.
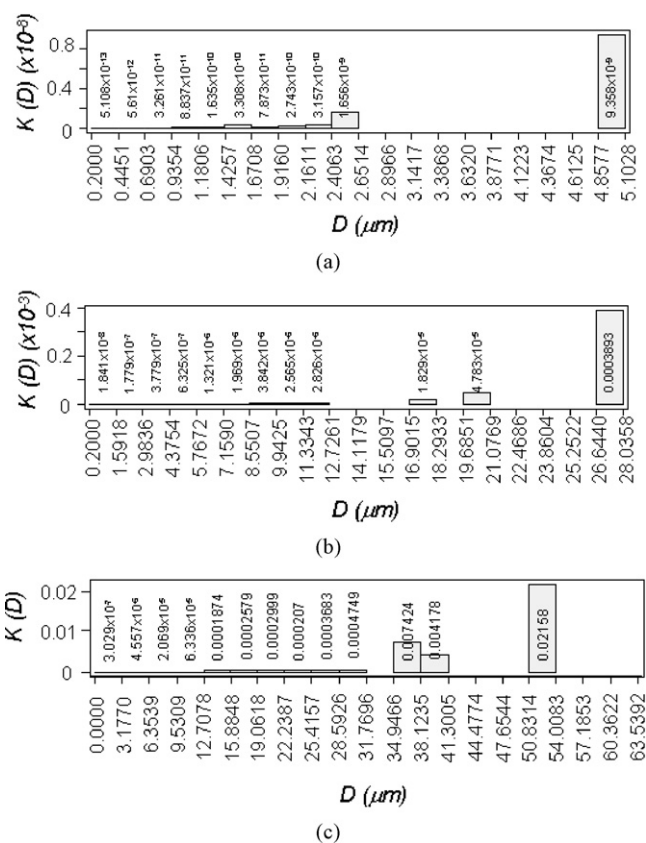

Fig. 11. STIMAN results as histograms of flocculated kaolinite partial pore contributions to filtration at pH 4 (a), at pH 8 (b), and in Ca(II) electrolyte (c).

bounded excluding those open to the edges of the micrograph region. The micrograph series of 5 magnifications across 500–8000× were used to calculate these microstructural parameters.

The data show that, at pH 8, the highest settling rate corresponds to the lowest total porosity and, importantly, the lowest open porosity. Closed porosity is similar across pH 6 and 8. Comparison of the filtration calculated from the Darcian inter-aggregate theory [18,19] as presented in Eq. (2) above, using the measured hindered settling rate and viscosity of the sample, with the intra-aggregate filtration calculated from the STIMAN analysis is shown in Fig. 10. Note that the filtration scale is logarithmic so that the differences between indices and between pH values are larger in absolute numbers. This analysis shows that the Darcian inter-aggregate filtration is similar in value to STIMAN calculated filtration for most of the pH range except between pH 6.5–9.5. In this pH interval, Darcian filtration trends oppositely from the intra-aggregate porosity calculated from SEM images and the settling rate reaches its highest value in suspension. This corresponds with the densest aggregates characterized by the lowest porosity in the sediment bed. The filtration values are likely to be most closely related to primary dewatering and bed density, which shows a maximum at pH 8. However, the intra-aggregate filtration, likely to be most representative of the trapped residual water in the settled bed, has a shallow minimum at pH 8. This filtration (intra-aggregate porosity) is particularly low and water is trapped in these small pores. The aggregates at pH 4 (Fig. 6a) apparently contain very little void space at this scale.

The porosity factor has a strong influence on floc permeability. More porous flocs with low density and low initial settling rate have higher filtration than compacted low-porosity, dense flocs that settle fast. This view is supported by correlating the maximum settling rate and minimum (total and open) intra-aggregate porosity with minimum intra-aggregate filtration calculated in STIMAN.

Graphs of partial void contributions to filtration in STIMAN estimates (Fig. 11) also show that it is not total porosity that counts in filtration but the abundance of larger intra-aggregate voids that plays the crucial role. At pH 4, the largest pores are ∼5 μm compared with the largest pores at pH 8 of 28 μm. The larger filtration at pH 10 is governed by channels up to 40 μm in diameter.

In the presence of Ca(II) ions with flocculant the aggregate histogram of partial pores contributing to filtration (Fig. 11c), shows a significant contribution from 35–55 μm diameter pores. This provides the largest filtration (Table 1).

The combination of a very compact intra-aggregates structure with large volume pores inter-aggregates makes the porosity value lower, which significantly enhances initial settling rate and filtration capabilities.

5. Summary

The settling characteristics, aggregate structures and their porosity/filtration/water retention of kaolinite have been studied through the settling process to bed formation. The initial kaolinite consists of pseudo-hexagonal platelets 50–200 nm in diameter, thickness of 160 nm and aspect ratio of ∼12. Quantitative cryo-SEM image analysis shows 3 stages in the mechanism of primary dewatering of kaolinite at pH 8. Initially, edge–edge (EE) and edge–face (EF) inter-particle associations form as open, loose aggregates. After some induction time, settling starts. The aggregates are now arranged into chain-like structures of EE and stairstep face–face (FF) associations. In the third stage, individual platelets in EE and FF stepped arrangements as chains, appear to slide across each other to more FF structures forcing the chain aggregates to contract. This contraction leads to fragmentation of the previously extended network and formation of more compacted aggregates.

Table 1
STIMAN calculated parameters from SEM images shows differences in porosity, filtration and initial settling rate in kaolinite suspension when monovalent and divalent ions are present in solution.

Sample	Kaolin Na, pH 8	Kaolin Na, A-130 pH 8	Kaolin Ca, pH 8	Kaolin Ca, A-130 pH 8
Porosity, two-dimensional from STIMAN (%)	79.7	40.4	80	56.6
Filtration (m/h)	1.7E−9	1.7E−4	7.5E−7	1E−3
Initial settling rate (m/h)	0.02	29.4	0.013	34

During settling, the sponge-like network structure with EE and FF string-like aggregates, limits dewatering because the steric effects in the resulting partially-gelled aggregate structures are dominant.

The addition of flocculant preserves the pre-existing microstructure by bridging the existing aggregates which come in contact with each other without significantly altering their internal structure. The effect of the flocculant is proposed to primarily link the aggregates, making them larger but lock in the intra-aggregate pre-existing structure. This effect also may fragment the extended network and allow the suspension to sediment faster at least until the gel point is reached. This lowers the total porosity within pH interval 6.5–9.5 and implies an increase in the Darcian filtration (Fig. 10).

In Na(I)-based electrolyte and at initial pH values ranging from 4 to 10 before flocculant addition, kaolinite builds a very high void ratio structure where individual platelets are largely EE oriented or present as separate chain aggregates. The chain aggregates are a few μm long but often only a single kaolinite platelet in thickness. When the pH is increased to 8, the long chained aggregates appear be thicken and exist predominantly in a stair-step FF particle orientation. EF orientation is rare. In Ca(II)-based electrolyte, the aggregate shape is significantly different. Aggregates are less elongated and rather irregular with a range of platelet orientations with EF as the preference. The filtration is highest in Ca(II)-based electrolyte (Fig. 11c) in spite of a moderate total porosity value (Table 1). Once again large numbers of high hydraulic radii pores have a deciding influence on the inter-aggregate filtration.

The effectiveness of water release from within aggregates of the network skeleton depends on the system permeability and can be characterized from both settling rates and porosity measurement. After network fragmentation and floc formation, the suspension consists of two different structural environments in the system which differs in filtration values:

- denser flocs consisting of aggregates with their internal filtration calculated from cryo-SEM micrographs;
- solution space between flocs and aggregates where filtration is characterized by the Darcy formula based on hindered settling rate.

Knowing that flocculant addition has little influence on the intra-aggregate structure, these results show that it is necessary to control the aggregate structures prior to the flocculant addition in order to achieve maximum water release.

References

[1] B.V. Derjaguin, L.D. Landau, Acta Physicochim. USSR 14 (1941) 633–652.
[2] E.J.W. Verwey, J.Th.G. Overbeek, The Theory of Stability of Lyophobic Colloids, Elsevier, Amsterdam, Netherlands, 1948.
[3] R. Hogg, Int. J. Miner. Process. 58 (2000) 223–236.
[4] M. Zbik, R.St.C. Smart, Clays Clay Miner. 46 (1998) 153–160.
[5] M. Zbik, R.St.C. Smart, in: H. Kodama, A.R. Mermut, J.K. Torrance (Eds.), Clays for Our Future, Proceedings of the 11th International Clay Conference, Pub. ICC97 Ottawa, Canada, 1999, pp. 361–366.
[6] M. Żbik, Clay Sci. 12 (Suppl. 2) (2006) 31–36.
[7] M. Żbik, Colloids Surf. A Physicochem. Eng. Aspects 287 (2006) 191–196.
[8] Y.M. Sergeev, G.V. Spivak, A.Y. Sasov, V.I. Osipov, V.N. Sokolov, E.I. Rau, J. Microsc. 135 (1983) 1–12.
[9] Y.M. Sergeev, G.V. Spivak, A.Y. Sasov, V.I. Osipov, V.N. Sokolov, E.I. Rau, J. Microsc. 135 (1) (1983) 13–24.
[10] V.N. Sokolov, D.I. Yurkovets, O.V. Ragulina, V.N. Mel'nik, J. Surf. Invest. X-Ray Synchrotron Neutron Tech. 14 (1998) 33–41.
[11] V.N. Sokolov, D.I. Yurkovets, O.V. Ragulina, V.N. Mel'nik, Bull. Russ. Acad. Sci. Phys. 68 (2004) 1491–1497.
[12] V.N. Sokolov, V.A. Kuzmin, Bull. Russ. Acad. Sci. Phys. 57 (8) (1993) 1386–1390.
[13] V.N. Sokolov, O.V. Razgulina, D.I. Yurkovets, M.S. Chernov, J. Surf. Invest. X-Ray Synchrotron Neutron Tech. 1 (4) (2007) 417–422.
[14] R.St.C. Smart, M. Żbik, G.M. Morris, in: J.S. Laskowski (Ed.), Proc. Fifth UBC-McGill Int. Conf. Fundamentals of Mineral Processing, Canadian Inst. Mining, Metallurgy and Petroleum, 2004, ISBN 1-894475-52-6, pp. 215–228.
[15] R.L. Frost, S.J. van Der Gaast, M. Żbik, J.T. Kloprogge, G.N. Paroz, Appl. Clay Sci. 20 (2002) 177–187.
[16] B. Braggs, D. Fornasiero, J. Ralston, R.St.C. Smart, Clays Clay Miner. 42 (1994) 123–136.
[17] B.J. Battersby, J.C.W. Sharp, R.I. Webb, G.T. Barnes, Microscopy M1192 (1994) 914.
[18] R. Buscall, L.R. White, J. Chem. Soc. Faraday Trans. I 83 (1987) 873.
[19] R. de Kretser, P. Scales, Filtration 7 (1) (2007) 255.
[20] M.L. Taylor, G.E. Morris, P.G. Self, R.St.C. Smart, J. Colloid Interface Sci. 250 (1) (2002) 28–36.
[21] M.S. Nasser, A.E. James, Sep. Purif. Technol. 51 (2006) 10–17.
[22] H.R. Van Olphen, An Introduction to Clay Colloid Chemistry, Wiley, New York, 1977.
[23] J.N. Israelachvili, G.E. Adams, J. Chem. Soc. Faraday Trans. 74 (1978) 975–1001.
[24] V.G. Babak, V.N. Sokolov, Colloid J. USSR (Kolloid. Zh.) 48 (1986) 185–191.
[25] N.R. O'Brien, J. Electron Microsc. 19 (1970) 277.
[26] N.R. O'Brien, Clays Clay Miner. 19 (1971) 353–359.